In-situ TEM characterization and atomistic simulation of cavity generation and interaction in tungsten at 800 °C under dual W^{2+}/He^{+} irradiation

Yildirim, E.; Mummery, Paul M.; Greaves, G; Race, C.P.; Jimenez-Melero, Enrique

DOI:
10.1016/j.nme.2024.101672

Nuclear Materials and Energy 39 (2024) 101672

Contents lists available at ScienceDirect

Nuclear Materials and Energy

journal homepage: www.elsevier.com/locate/nme

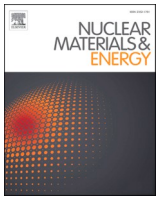

In-situ TEM characterization and atomistic simulation of cavity generation and interaction in tungsten at 800 °C under dual W^{2+}/He^{+} irradiation

E. Yildirim [a,b,*], P.M. Mummery [b], G. Greaves [c], C.P. Race [e], E. Jimenez-Melero [a,d,*]

[a] Department of Materials, The University of Manchester, Manchester M13 9PL, United Kingdom
[b] School of Engineering, The University of Manchester, Manchester M13 9PL, United Kingdom
[c] School of Computing and Engineering, University of Huddersfield, Huddersfield HD1 3DR, Yorkshire, United Kingdom
[d] School of Metallurgy and Materials, University of Birmingham, Birmingham B15 2TT, United Kingdom
[e] Department of Materials Science and Engineering, University of Sheffield, Sheffield S10 2TN, United Kingdom

ARTICLE INFO

Keywords:
Tungsten
Dual ion irradiations
In-situ TEM
Radiation-induced cavities
Molecular dynamics simulations

ABSTRACT

In this work, we have investigated the role of pre-existing nano-scale cavities and irradiation sequence in helium clustering, and in the evolution of the cavity population in tungsten at 800 °C, by performing in-situ Transmission Electron Microscopy (TEM) characterizations under dual-beam W^{2+}(600 keV)/He^{+}(10 keV) irradiation to a total dose of 0.351 dpa, and supported by atomistic simulations. Pre-existing cavities, induced by single W^{2+} irradiation to 0.256 dpa, were seen to attract induced defects from subsequent irradiations, resulting in enhanced cavity size and a reduced number density in sequential irradiation when compared to concurrent irradiation. Such cavities developed faceted geometries and saturated in number density at an additional 0.051 dpa induced by He^{+} exposure in the sequential irradiation. In contrast, concurrent irradiations generate a denser cavity distribution that showed no sign of saturation or faceting up to the total irradiation damage of 0.351 dpa. In addition, Molecular Dynamics and Statics simulations were performed using LAMMPS software. These showed the pre-existing cavities to be trapping sites for helium atoms. Despite the large binding energy of ~6 eV of those cavities, He-He interactions still occurred beyond the effective radius of such sinks, leading to additional He-He clustering not seeded by neighbouring cavities. These results point to the importance of selecting the irradiation conditions to simulate synergistic ion effects on cavity formation and evolution in plasma-facing tungsten-base materials.

1. Introduction

Tungsten (W) is currently the frontrunner candidate as armor material for plasma-facing components in fusion devices, including in the divertor region [1–3], where it will experience high particle fluxes and steady-state heat loads ranging from ~8–20 MWm^{-2}. These local conditions will generate W surface temperatures ≥800 °C [4], together with predicted radiation-induced dose levels of ~0.1 dpa for the first ITER divertor [5] and dose rates of ~3 dpa/fpy in the divertor and up to 9dp/fpy at the first wall for DEMO plasma-facing W components [6–7].

Energetic He particles impinge on the divertor surface at low energies, <100 eV, but alpha particles in the keV range can also be present at both the divertor and the first wall due to alpha particle loss form the separatrix and core [8–10]. These He atoms can diffuse and agglomerate into nano-scale bubbles within the tungsten matrix, reducing the material's ductility and degrading its thermal properties over time [11–14]. He atoms present a special affinity for vacancies in the W lattice [15–17], with these vacancies either present thermally in the structure or formed during the neutron- or He-induced displacement cascade. Consequently, He-vacancy complexes are generated as early precursors of bubble formation. Vacancy characteristics in tungsten have been probed to demonstrate monovacancy mobility at 350 °C [18,19] and stable voids at 800 °C, which order into extended void lattices at higher fluences [20–23]. Thermal or fast neutron fluxes produce both dislocation loops and voids (both <10 nm in diameter) at ≤750 °C, whereas at higher temperatures the microstructure is characterized primarily by larger voids (>10 nm) [24–27]. There are additionally Re and Os produced through transmutation, forming nano-scale solute clusters or precipitates, and decorate dislocations and grain boundaries [28].

* Corresponding authors at: Department of Materials, The University of Manchester, Manchester M13 9PL, United Kingdom.
E-mail addresses: emre.yildirim@manchester.ac.uk (E. Yildirim), e.jimenez-melero@bham.ac.uk (E. Jimenez-Melero).

https://doi.org/10.1016/j.nme.2024.101672
Received 16 January 2024; Received in revised form 9 May 2024; Accepted 10 May 2024
Available online 11 May 2024

Ion beams available at linear and cyclotron facilities can be used to emulate the effects of neutron irradiation in structural materials. When these are coupled with *in-situ* Transmission Electron Microscopy (TEM) studies, defect generation and accumulation can be monitored in real time as a function of ion fluence [29–33]. In-situ TEM characterizations under single He^+ irradiations have revealed the formation of nano-sized He bubbles, simultaneously with mixed vacancy/interstitial dislocation loops with a Burgers vector $\mathbf{b} = \pm 1/2\langle 1\,1\,1\rangle$, from room temperature up to ~800 °C [34,35]. Less mobile $\mathbf{b} = \langle 1\,0\,0\rangle$ dislocation loops (<20 % of the total loop fraction) have also been observed at temperatures ~450–700 °C, formed either by interactions between high-density He clusters or by the reaction of two $\mathbf{b} = \pm 1/2\langle 1\,1\,1\rangle$ loop variants [36]. The $\mathbf{b} = \pm 1/2\langle 1\,1\,1\rangle$ loop mobility seemed to be inhibited by the presence of He interstitials in the lattice [35,37]. Large (~5–10 nm) loops at 600–800 °C can evolve into tangled networks [34] or elongated rafts [38].

The diameter of helium bubbles formed under irradiation increases with temperature at 800–1000 °C [35,39,40], and larger faceted bubbles (≤10 nm) are detected along grain boundaries at 950 °C [40,41]. Moreover, sequential dual-beam irradiations of coarse-grained W at 950 °C with Kr^{2+} and He^+ revealed the annihilation of dislocation loops, initially produced by Kr^{2+}-induced cascades, by defects produced in the early stages of a subsequent He^+ irradiation. This was followed by the nucleation of new dislocation loops and loop rafting, due to the He implantation. However, this loop annihilation process did not occur when irradiating W simultaneously with Kr^{2+} and He^+ at that temperature thus exemplifying the effect of irradiation sequence. The number density of bubbles at the end of the irradiation campaign was similar for both sequences of irradiation, although a smaller average value of bubble diameter was measured in case of sequential irradiation [42].

To investigate the He interaction with voids in tungsten, and to further view the potential impact of the type of irradiation sequence, in-situ TEM experiments were performed in this study, supported by both Molecular Dynamics (MD) and Molecular Statics (MS) simulations. This work encompasses the use of W^{2+} and He^+ ions in both concurrent and sequential irradiations at 800 °C and in-situ monitoring of the microstructure evolution, with the focus on the void/bubble formation throughout the irradiation campaign. Additionally, MD simulations, alongside complementary MS simulations, were pursued to further study the effects of vacancy and void formation on the initial He clustering within the W microstructure.

2. Experimental

2.1. In-situ TEM under irradiation

As part of a wider program on W-base alloys, as-received W rods from Alfa-Aesar (99.95 %, major impurities <30 ppm) were crushed, and subsequently melted and solidified in an arc melter. The material produced was subsequently machined into thin slices and ground to ~100 μm in thickness. X-ray fluorescence analysis yielded any detectable element other than W to be in a concentration <0.05 % (it should be noted that XRF cannot pick up C or O impurities). The average grain size was ~1.5 mm. TEM discs of 3 mm in diameter were then punched from a thinned (<100 μm, SiC grinding paper p4000) and electropolished at −5 °C using an electrolyte containing 14 vol% H_2SO_4 and 84 vol% CH_3OH and a voltage of 20 V.

In-situ TEM experiments at 800 °C under irradiation, using 600 keV W^{2+} and 10 keV He^+ beams, were undertaken at the MIAMI-II TEM/ion accelerator facility of the University of Huddersfield [30]. The TEM disc was inserted into a double-tilt heating holder (Gatan Model 652), that uses a current flow through a Ta furnace surrounding the sample and heated to the target temperature until stability achieved (fluctuations ≪ 1 °C detected) before the start of ion irradiation. The temperature was measured via a thermocouple attached to the furnace near the sample surface. The sample was held in place by two Ta washers using a Hexring® clamping mechanism to ensure good thermal contact between the sample and the furnace. The irradiation parameters are shown in Table 1. The damage and implantation profiles were calculated using the *Stopping and Range of Ions in Matter* (SRIM-13) software [43,44] with the quick Kinchin-Pease method [45], an average displacement energy of 90 eV for W [46] and default values for other software settings. The total damage level achieved by each type of ions was 0.256 dpa (W^{2+}) and 0.095 dpa (He^+). The total He concentration was 36,500appm, giving a final He:dpa ratio of ~104,000 He/dpa. The dose profiles and implanted ions can be seen in Fig. 1 where the central area of the ~60 nm sample was taken to account for surface affects with the doses being produced as per the method in Stoller *et al.* [45].

To evaluate the effect of the sequence of irradiation on the structure evolution in W, we carried out a sequential ('SQN') irradiation at 800 °C using first a 600 keV W^{2+} beam until a total damage level of 0.256 dpa was achieved. Afterwards, the W^{2+} beam was switched off while the disc was kept at 800 °C. The disc was then immediately irradiated by a 10 keV He^+ beam with an additional 0.095 dpa and 36,500 appm He, before switching off the beam and cooling the sample back to room temperature. In a separate experiment, an equivalent sample was subject to a concurrent ('CON') irradiation with a W^{2+} beam (600 keV) and a He^+ beam (10 keV) at 800 °C to a total damage level of 0.351 dpa and the 36,500 appm (with the same ratio as in the SQN irradiation). Table 1 describes the flux and fluence of each irradiation, and the respective damage and appm of He implanted in the samples.

For *in-situ* imaging during irradiation, a Hitachi H-9500 TEM with a 300 kV acceleration voltage was used at the Huddersfield facility. Micrographs were recorded off zone axes for better cavity contrast, during stepwise increase in ion fluence. An integrated EELS system allowed us to determine the sample thickness in the region of interest prior to the heating/irradiation cycle [47]. The sample thickness was ~60 nm. The incoming W^{2+}/He^+ ion beams were at an angle of 18.7° with respect to the electron beam in the TEM. Additionally, post-mortem TEM analysis of the *in-situ* irradiated samples was carried out *ex-situ* using FEI Tecnai TF30 microscope also operating at a voltage of 300 kV.

Cavities (used to refer to voids and/or bubbles produce during irradiation) were imaged with the "out-of-focus" Fresnel imaging technique, where they are detected as black dots with bright fringes in over-focussed images, and the opposite in under-focus conditions [48]. All images were taken with a defocus value of $\Delta f = \pm 500$ nm, and in the bright-field (BF) condition. The number density and average size of the cavity distribution for *in-situ* irradiation were determined using the whole single frames taken during the irradiations. For post-mortem *ex-situ* characterization, the samples were further analysed for the same values at higher resolution and at multiple areas across the foil. Five frames per sample covering 70 nm^2/frame were taken for each sample. These images were analysed using image filtering and processing with ImageJ software [49] to automatically count and size the cavities, thus reducing possible human error and maintaining consistency across samples. The analysis sequence is captured in more detail in Fig. S.1 the Suppl. Material.

2.2. MD and MS simulations

To support the dual-beam irradiation campaign, Molecular Dynamics (MD) simulations were performed using the LAMMPS software [50,51]. The simulation cell consisted of a $40a \times 40a \times 40a$ box with 128,000 atoms and periodic boundary conditions (a being the lattice parameter of 3.165 Å). The relevant interatomic potentials were accessed from the Interatomic Potential Repository (https://www.ctcms.nist.gov/potentials/). For W-W interaction, a potential from Mason et al. [52] was used, W-He interaction from Juslin and Wirth [53] and He-He interaction from a Beck potential modified by Morishita *et al.* [54]. This collection of potentials has been shown to reproduce reliably the *ab-initio* interaction energy for helium, tungsten and vacancy mixed interactions [55,56]. Each simulation was performed on LAMMPS

Table 1
Experimental parameters used during the *in-situ* sequential (SEQ) and concurrent (CON) irradiation of tungsten (W), together with the average cavity diameter and number density measured *ex-situ*at room temperature at the end of the dual beam irradiation. The dose (dpa) and He content (appm) was taken from the middle third of the 60 nm specimen to account for surface affects.

Irradiation sequence	Time (s)	Flux (m^{-2} s^{-1})	Damage (dpa)	He (appm)	Ion energy (keV)	Average diameter (nm)	Number density (10^{23} m^{-3})
WSQN	800	7×10^{14}	0.256	–	600 W^{2+}	2.0 ± 0.6	6.7 ± 0.6
	660	2×10^{17}	0.095	36,500	10 He^{+}		
WCON	800	7×10^{14}	0.351	36,500	600 W^{2+}	1.7 ± 0.5	11.1 ± 0.7
		1.7×10^{17}			10 He^{+}		

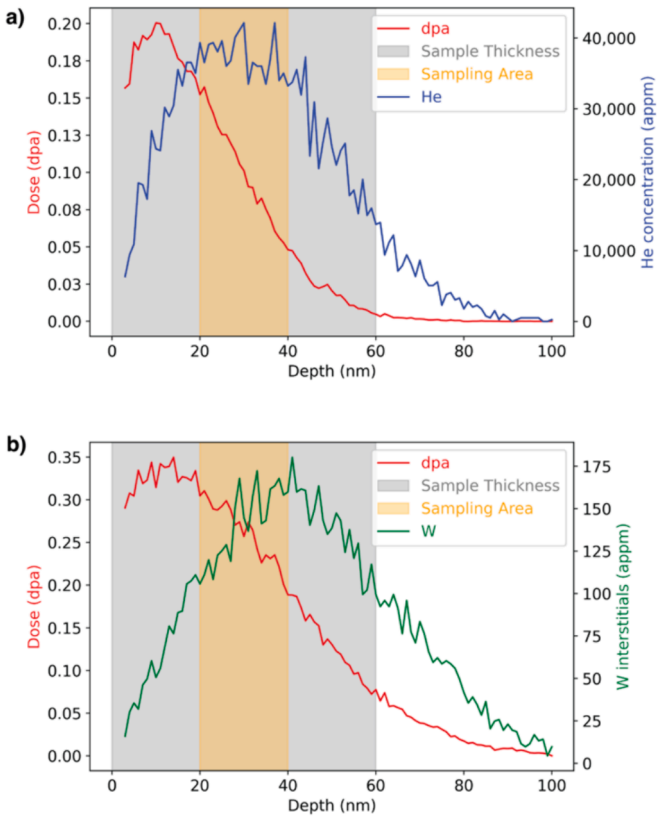

Fig. 1. SRIM calculations detailing the sample thickness and the sampling area, with the latter being the chosen area for the dpa and He concentration calculations, to account for denuded zones due to surface image forces.

version 29-Sep-2021 on 48 cores using the Computational Shared Facility at the University of Manchester.

The aim of the MD simulations was to assess the helium interaction with either pre-existing void structures or single vacancies distributed throughout the lattice, mimicking the pre-damage causing void formation in sequential (SQN) irradiations or the more evenly distributed vacancies that would be generated in concurrent (CON) irradiations, respectively. For the SQN irradiation, the starting structure contained spherical voids of radius 2*a* giving a number density of ~10^{25} m^{-3}. This gives 10 voids in the simulation box. This structure was used to represent void structures formed under single W^{2+} irradiation and prior to He^{+} beam exposure of the W material and is hereafter referred to as the voided (V) structure. For the CON irradiation, a finer distribution of vacancies was created by randomly removing atoms from the lattice to a 0.5 % initial porosity, "porosity" here being a LAMMPS command that randomly deletes a set percentage of the atoms in the simulations box. This is termed the porous (P) structure. This finer distribution was representative of the concurrent irradiation, where radiation-induced vacancy formation and He implantation would take place simultaneously with the W^{2+}/He^{+} bombardment, and thus vacancies would be distributed throughout the lattice. While self-interstitial atoms would still be produced in the irradiations, the higher He-vac interaction energies than He-SIA [57] meant these were the focus of these simulations. For both type of simulations, 650 atoms per run were removed by either void formation or random atom removal. The locations of the voids and the random vacancies were varied across four different simulations, and the final values were averaged for each type of simulation. Helium was inserted at random locations every 10 ps (giving an equivalent flux of ~6.24×10^{26} $m^{-2}s^{-1}$) up to a total 6.4 ns totalling 640 atoms (0.5 at%). Each simulation was run at 800 °C (1073 K) using a Nose-Hoover thermostat. The simulations results were visualised with the OVITO software [54], and a cluster analysis was carried out using the in-built cluster analysis tool with a cut-off distance of 1.1*a*. After completion of the simulations, the cluster datasets were combined to tally the cluster with the most He atoms in it (termed the largest cluster in later figures) for each run and the total cluster evolution with time. The starting structures for the MD simulations can be seen in Fig. 2.

Additionally, MS simulations were conducted to understand the effectiveness of pre-existing voids as sinks for He atoms. Voids with radius 1, 1.5 and 2*a* were generated in the simulation, with a helium atom inserted along the ⟨1 1 1⟩, ⟨0 1 1⟩ and ⟨0 0 1⟩ directions, at selected locations from the centre of the void in steps of 0.1*a* to a maximum distance of 5*a*. Each simulation was run 5 times with a different random number seed to account for any variation in location caused by interaction of the inserted helium atom with tungsten atoms. The system was minimised before and after the helium insertion and the formation was recorded as per the equation below:

$$E_{formation} = E_f - \left(\frac{N_i + 1}{N_i} * E_i\right)$$

where E_f is the final total energy of the system, N_i is the initial number of atoms and E_i is the initial total energy of the system. The binding energy was then calculated by subtracting the energy of an equivalent system with the He atom at a very large distance from the void. These gave a tentative indication of the strength of voids as sinks for helium atoms. Each simulation used the minimise command and the potentials used were the same as the MD simulations described prior.

3. Results

3.1. Ion irradiations

Micrographs taken during the sequential and concurrent irradiations are shown in Fig. 3, respectively. During SQN irradiation, the initial W^{2+} irradiation to 0.256 dpa generated cavities in the W microstructure, with an average diameter of 1.2 ± 0.6 nm and a number density of 8×10^{-23} m^2. This can be seen in the first image of Fig. 2. During the subsequent He^{+} bombardment, there is a continuous increase in number density, with a saturation detected at ~0.051 dpa, whereas the average diameter rises gradually with He^{+}-induced damage level until a subtle drop takes place between 0.063 and 0.095 dpa, see Fig. 4a–b. The small drop in cavity size can be attributed to the cavities becoming faceted, and therefore their 2-D image in TEM appears smaller, despite a significant reduction in volume not occurring. In contrast, the CON irradiation is characterised by a weak, gradual increase up to the maximum damage level of 0.095 dpa. Due to the experimental conditions the values at

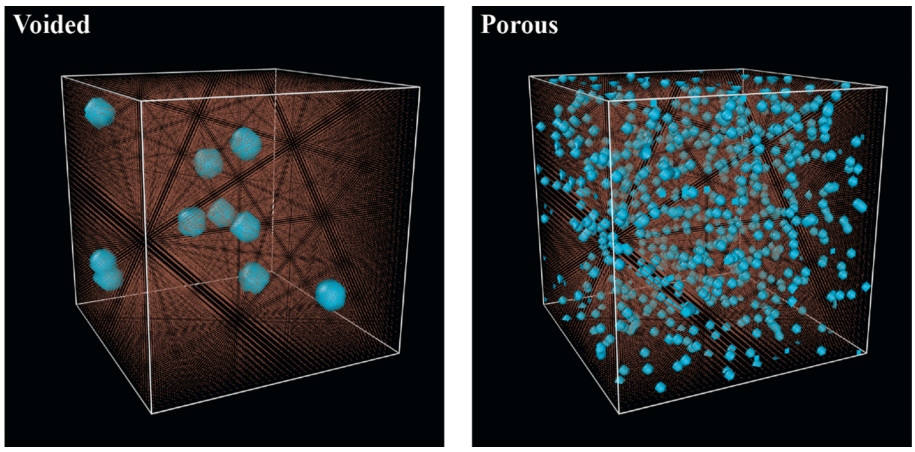

Fig. 2. Figure showing the two starting structures using the OVITO surface mapping function. The surface mapping function gives the surfaces of the voids and the vacancy sites in light blue while the matrix atoms are in orange and are reduced in size in the image to not obscure the surface structures. (For interpretation of the references to colour in this figure legend, the reader is referred to the web version of this article.)

measured at 0.013dpa were omitted due to a required change in viewing location. The average diameter of the radiation-induced cavities shows a simultaneous, weak increase throughout the irradiation, see Fig. 4c–d.

Fig. 5 shows representative micrographs of the final dual-beam irradiated W structure at 0.5 dpa, taken *ex-situ* at room temperature, together with the cavity size distribution for both irradiation sequences, based on five frames per sample covering 70 nm^2/frame at higher magnification than the *in-situ* micrographs as per the ImageJ methodology described in Section 2. The CON irradiation generates a finer population of cavities dispersed in the W microstructure, as compared to the SQN irradiation. In the latter case, two types of cavities can be observed, i.e. larger, less frequent, faceted cavities in addition to a set of smaller cavities. The final values of the average diameter and number density of cavities for both types of irradiation sequences are given in Table 1. The *ex-situ* micrographs reveal consistently a by of smaller cavities than those captured in situ during irradiation. Even though both types of irradiations reached a final damage level of 0.5 dpa, there are clear differences in the cavity population, characterised by an average diameter of 2.0 ± 0.6 nm (SQN) and 1.7 ± 0.5 nm (CON), whereas the final number density amounts to 6.7 × 10^{-23} m^{-2} (SQN) and 11.1 × 10^{-23} m^{-2} (CON), respectively.

3.2. Simulations

The evolution of He clustering in W throughout the MD simulations at 800 °C is shown in Fig. 6 for selected times, namely 1 ns, 3.2 ns (halfway) and 6.4 ns (final), or 1,000,000, 3,200,000 and 6,400,000 timesteps. The variation in total cluster number and number of He atoms in the largest cluster with simulation time is shown in Fig. 7, for a structure initially containing either porosity (P) or voids (V). These simulation results show limited He clustering in the more finely distributed vacancy population (P structure), with the largest cluster being five times smaller than the largest cluster in the voided cell (V structure) (see final values of the simulations in Table 2). The V structure, on the other hand, showed a higher number of large He clusters, together with a 55 % reduction in the final number of clusters as compared to the P structure. The cavity density of 10^{25} m^{-2} led to 10 cavities being present in the simulation cell of the V structure. The evolution of the cluster numbers revealed a higher number of clusters present than cavities, where He atoms were observed to cluster outside of the pre-existing voids or cavities, as well as being attracted to those cavities. This is exemplified in Fig. 8 showing helium clustering both in voids and inter-void spaces.

In addition, complementary MS simulations demonstrated a strong He-void binding energy for all void sizes tested. There was little difference in binding energy with void size, with all producing values of ~6 eV. The plots in Fig. 9 show the strong binding energy of these voids, with the radius of the void highlighted with a line cutting the *x*-axis. The larger the void, the larger the capture radius was, with a helium-free zone being shown in the top figure. As the void radius decreased, more intermediate binding energies appeared closer to the void edge, with the most being seen at the small void radius.

4. Discussion

4.1. Cavity behaviour during in-situ TEM irradiations

The cavity structures observed in the SQN irradiation underwent a marked increase in average diameter and number density with damage level. With vacancies mobile at 800 °C [58], cavities were formed during the initial exposure to the W^{2+} beam, those cavities grew with further He^{+} irradiation. Since vacancies possess a great affinity for He in W [59], agglomerated vacancies in the form of cavities acted as traps for incoming He ions. Vacancies generated by the He-irradiation-induced damage cascade also have an affinity for voids [60], and therefore these would also contribute to the void size increase.

As the temperatures of these irradiations are above Stage IV (720 °C [61]), helium, helium-vac and vacancy mobility are all possible. Despite this, the generation of defects during the irradiations would act to hinder some of this diffusion. Yang *et al.* [62] used Kinetic Monte Carlo (KMC) simulations to study He nucleation in tungsten with vacancy addition finding a reduction in the mobility of He with vacancy addition, with vacancy concentrations of 1–50 appm. This study found that at temperatures above Stage IV recovery there was a contribution of self-trapping of less than 50 % for both 1000 °C and 1200 °C simulated and vacancy-helium complexes nucleated the remaining clusters. The contribution of vac-impurity migration, a key feature of Stage IV [61], was not taken into account and therefore some mobility of these clusters would still feature at these temperatures. Despite this reduction in mobility, *in-situ* TEM work by Harrison *et al.* [35] has shown an increase in cavity size and a reduction in the number density moving from 500 °C to 750 °C suggesting increased mobility at Stage IV temperatures. Such an increase suggests more contributors to cavities (He, He-vac, vac etc.) are mobile at these temperatures, implying the generation of cavities in this study would have contribution from diffusive processes. Overall, this suggests a reduction in the mobility caused by the damage cascade in this study, but this reduction to not be sufficient to suggest the He implanted cannot interact with the defect structures present in the sample as well as the self-generated damage cascade. This is significant in the discussion of the sequential and concurrent irradiations, due to the different vacancy distributions in either study.

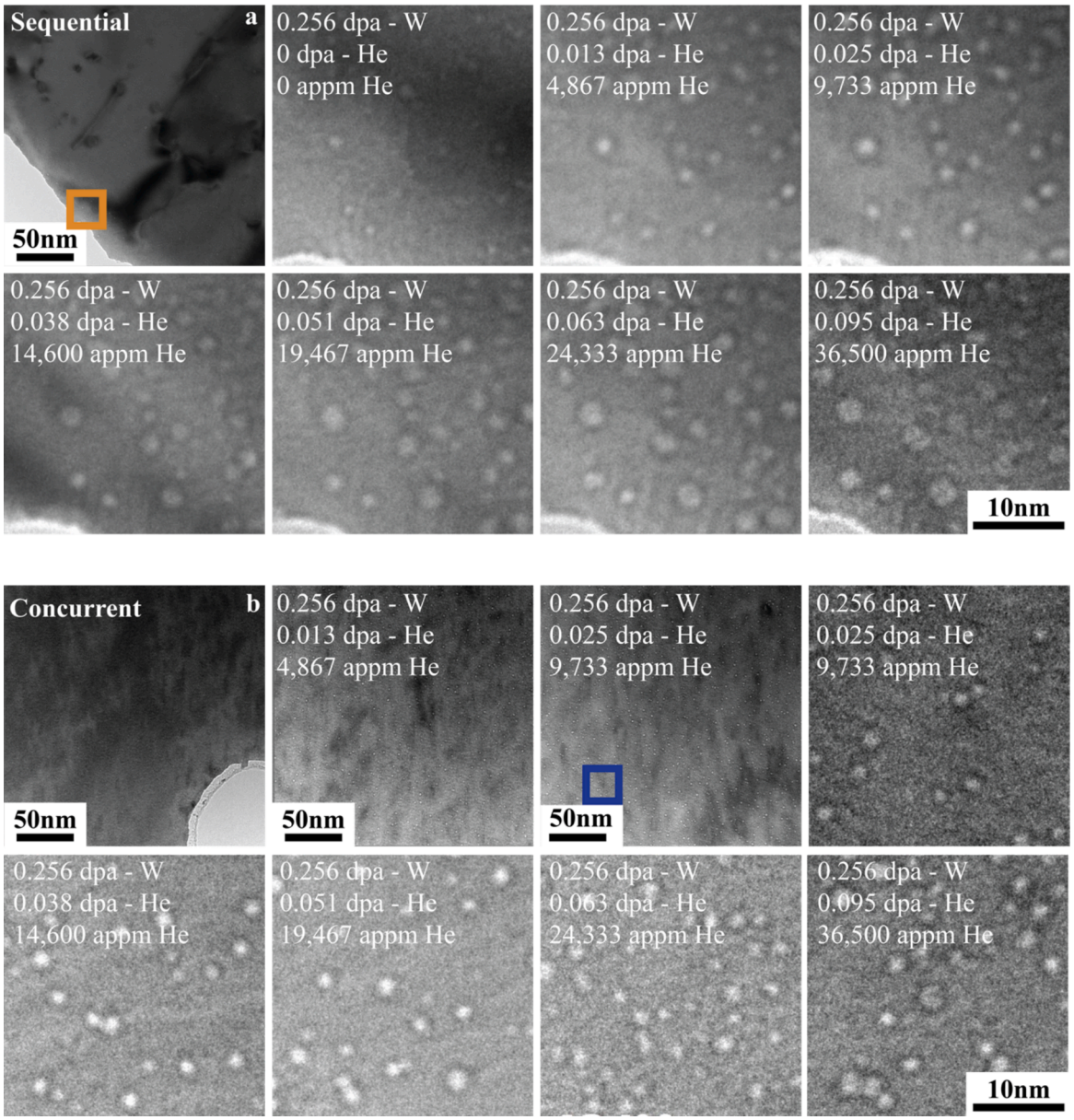

Fig. 3. (a) Evolution of the W microstructure during He^+ irradiation at 800 °C, up to an average He level of 36,500appm and 0.095dpa. The sample had undergone a prior irradiation by W^+ ions to 0.256 dpa. The initial location is highlighted, then digitally zoomed images follow showing the building of cavities. (b) Demonstrates a similar evolution in concurrent irradiations up to the full 36,500 appm He and a total dose from both W^{2+} & He^+ of 0.351 dpa (0.256 dpa from W^{2+} and 0.095 from He^+). Due to experimental conditions during the concurrent irradiations, the location for the concurrent irradiation was changed after the first and second image, this data is excluded from the latter quantitative analysis and the digital zooms are taken only on the relevant dose levels.

The cavity growth in Fig. 2 shows such interactions in practice with the pre-existing cavities growing and faceting during the irradiation demonstrating the mobility of the defects created and He injected in the sample. There is an increase in cavity number density, consistent with a higher number of resolvable cavities becoming visible, which begins to level off at 0.051 dpa. The observed saturation in number density is an order of magnitude higher than a comparable single 40 keV He ion irradiation study at 800 °C, with saturation taking place at 0.2 dpa [38]. Due to the W^+ beam in this study there are more defects present, a higher number density would be consistent with the increased presence of vacancies as trapping sites for helium in this study, thus pinning the helium and reducing overall agglomeration.

In the CON irradiations, there was also a steady increase in number density with increasing dose. This value was found to be lower for defects detected at the *in-situ* magnification. *Ex-situ* measurements taken in the post-mortem analysis of these samples, in contrast, confirmed the number density for the concurrent irradiations to be significantly higher than the SQN as seen in Fig. 5. This may be due to the smaller cavities in the CON irradiations, meaning the higher magnification images could not resolve the smaller defects with sufficient precision. The average cavity diameter slowly increases as He atoms and further vacancies are attracted to the already formed cavities. This increase is at a much lower rate than the SQN irradiations, most likely due to the reduced mobility of the small He-vac clusters [63] where He atoms were being pinned by defects and other He atoms in the matrix. The number density showed no clear evidence of saturation $\leq$0.095 dpa from He and 36,500 appm He.

The final cavity density and average diameter are markedly different between the two sets of irradiations. The pre-damaged SQN sample had agglomerated vacancies in the form of voids, whereas the concurrent irradiations had vacancies present in more even quantities throughout the sample. The formation of smaller cavities is consistent with reported

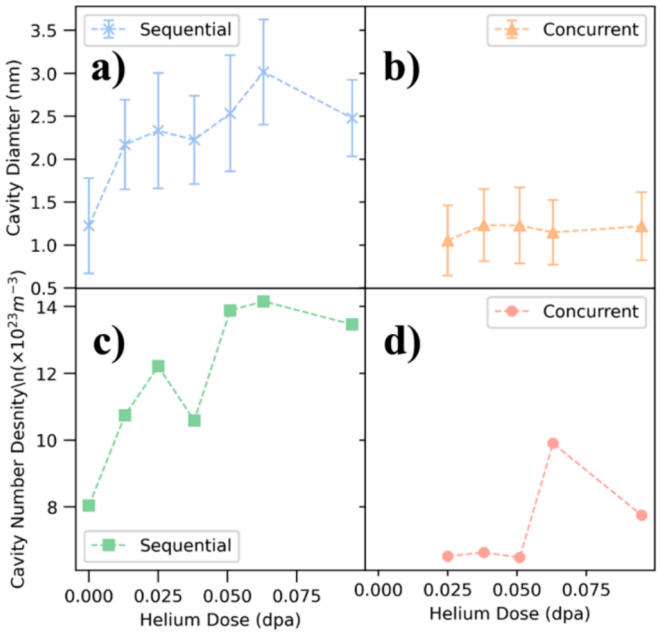

Fig. 4. Variation of the average diameter and number density of bubbles in the W microstructure at 800 °C, with increasing He^{+}-induced damage level (dpa) for (a)–(b) sequential and (c)–(d) concurrent W^{2+} & He^{+} irradiation. Note due to experimental conditions, the imaging site had to be changed and therefore values from the first 0.013dpa of the concurrent irradiation have been omitted. Variation in bubble size per frame is captured by standard deviations from one sigma values, while number density is only taken from the single frame imaged during the irradiation.

DFT and experimental work [59,64,65] which showed He readily occupying available sites in W; such sites would be formed and distributed throughout the lattice in the CON irradiation thus reducing He mobility. Pre-existing cavities in the SQN irradiation would act to trap local He and mobile vacancies and SIAs, thus leading to less of these defects present in the intra-cavity spaces. Without these, He would be more mobile in these intra-cavity spaces. This would lead to more clusters of He therefore reducing their number density and increasing their size. Further accumulation of vacancies at the voids would have also increased their size and further limit smaller, more frequent, cluster formation.

Injected self-interstitials from the W^{2+} beam could also contribute to these differences. Additional SIA-He complexes could form, and this would be more pronounced in CON irradiations. The mobility of the He-vac complex could be affected by these additional SIAs, in addition to the vacancies and SIAs generated from the damage cascade, therefore contributing to the higher number density in the CON irradiation. The SQN work, on the other hand, contained nucleation sites for cavity growth due to the cavities that had been formed in the initial single ion irradiation, which may have further been sinks for the injected SIAs. To isolate whether these effects observed in this study were due to injected SIAs, the following simulations were performed.

4.2. Cavity evolution in MD and MS simulations

Helium atoms within the MD simulations were mobile and clustered due to the high He-He affinity and He-vac interaction. These conditions revealed two additional effects in the cavity distributions and evolution in the two types of irradiations. First, the V structure promoted a higher degree of He clustering, consistent with the larger cavity structure observed in the SQN irradiation. This was further demonstrated by the

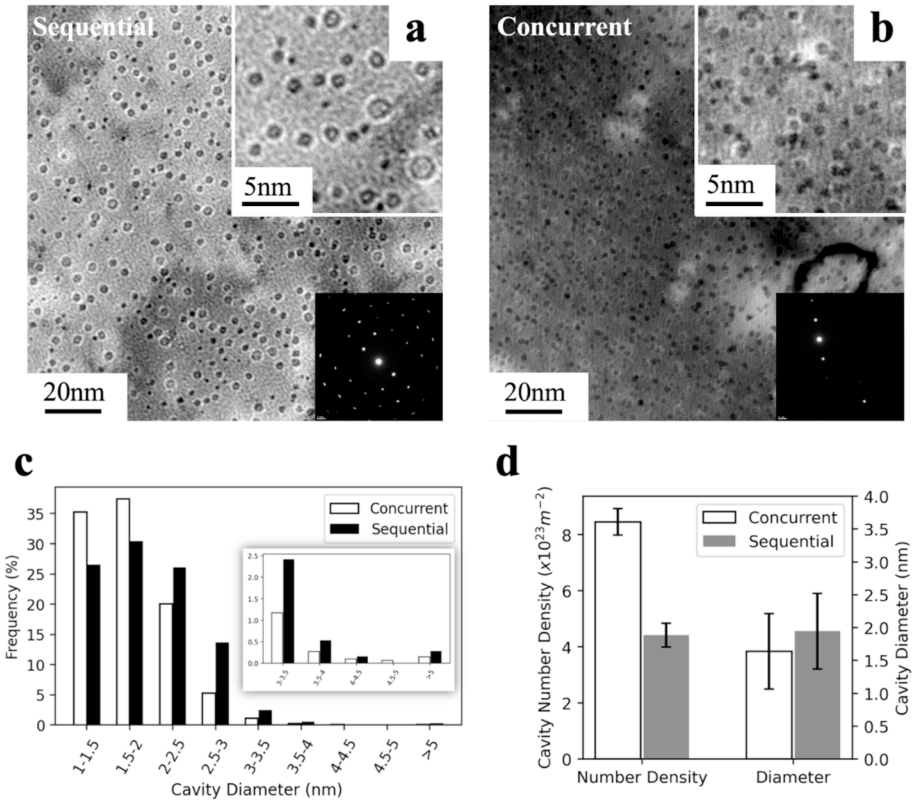

Fig. 5. Representative micrographs of the dual ion irradiated W structure characterized ex-situ at room temperature, after having been subject to W^{2+} and He^{+} irradiation at 800 °C up to a total damage level of 0.351 dpa during (a) sequential and (b) concurrent irradiation. (c) Bubble size distribution for both irradiation sequences, based on five frames per sample covering 70 nm^2/frame with (d) showing the number density and average sizes of the cavities. One sigma standard deviations account for variation across each frame is included as error bars.

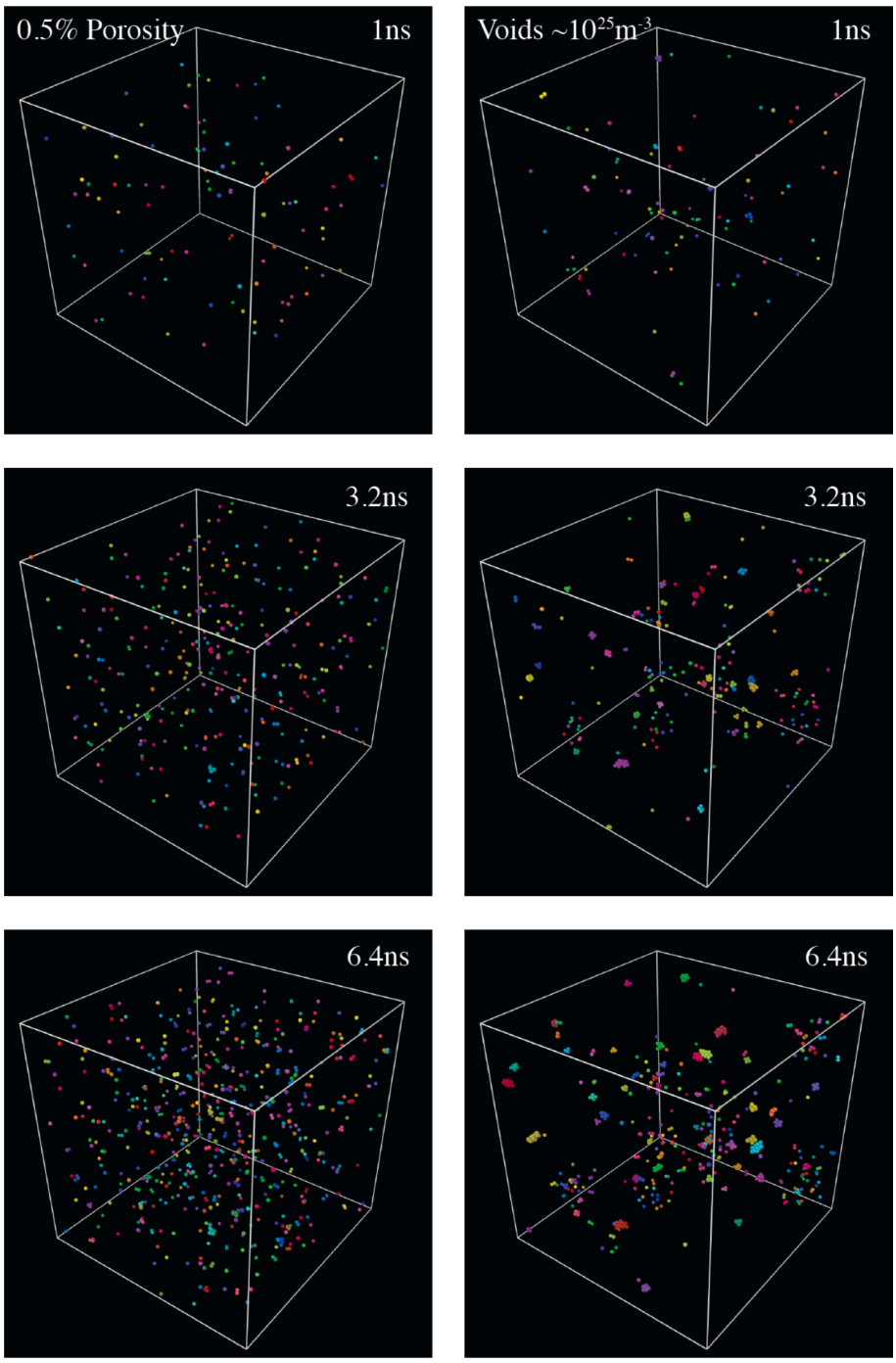

Fig. 6. Evolution of He clustering in W throughout the molecular dynamics simulation at 800 °C for selected computing times. The initial structure for the simulation contained a porosity level of 0.5 % (left column) or voids of radius 2*a* giving a number density of $\sim 10^{25}$ m^{-3} (right column), being representative of concurrent or sequential (W^{2+} and He^{+}) irradiations, respectively.

high binding energy of the void seen in the MS simulations. In the P structure, in contrast, He atoms are trapped by single vacancies or small vacancy clusters present in the lattice. This is consistent with the greater number density of cavities seen in the CON irradiations. Growth of these small clusters by further incorporation of He atoms was observed as the He was still mobile, but this mobility was reduced. This He-vacancy affinity is a well-known interaction [15,66] and clearly plays a dominant role in these simulations in slowing the He mobility and hindering cavity growth.

Additionally, the second observation was the formation of He-He clusters in the intra-void regions through self-affinity in the V structure, despite the presence of pre-formed voids. This suggests the formation of additional cavities in the SQN irradiations may have not been nucleated from the pre-existing cavities from the first irradiation, with these then growing with further exposure to the He^{+} beam. This is consistent with He atoms not necessarily requiring the presence of vacancies to nucleate an immobile cluster, rather when attaining sufficient size they immobilise by punching out an SIA forming a He/vac cluster [53]. Additionally, it suggests that the range of the void interaction is not large enough to inhibit this He-He interaction. The mobility of the He atoms in between the cavities would therefore be higher as they are also not inhibited by the presence of defects in these spaces. MS

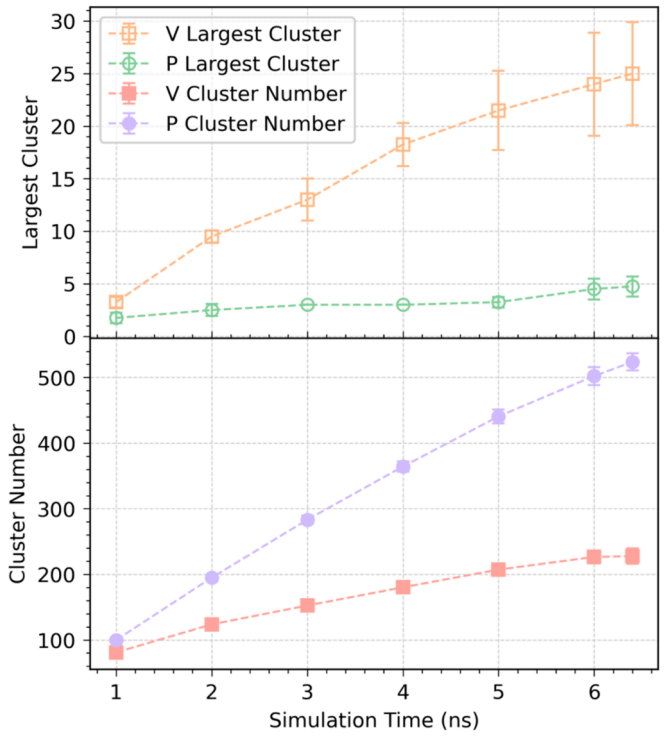

Fig. 7. Variation in total cluster number and number of He atoms in the largest cluster with simulation time in the case of an initial structure containing 0.5 % porosity (P) or voids with a number density of ~10^{25} m^{-3} (V). To distinguish different clusters, each cluster has been coloured differently in the cell, while the tungsten atoms have been deleted.

Table 2
Final cluster distribution obtained in the molecular dynamics simulations after injection with 640 He atoms in W for the two starting simulation structures, namely void (sequential irradiation) and porous (concurrent irradiation).

Structure	Cluster number	Largest number of He atoms in a cluster
Void	228 ± 11.8	25 ± 4.9
Porous	532 ± 13.2	5 ± 0.96

simulations confirm the short range of the cavity interaction with a high binding energy being seen close to the void, but this rapidly falling off as the distance from the void increases. These simulations also showed an increasing trapping radius with increasing cavity size. If the void is assumed to be a free surface, this may be due to an increased volume relaxation with increasing void size would give an increased image interaction and, thus, increasing capture radius.

The value of 6 eV for the binding energy well recreated the trend seen in the original Juslin & Wirth [53] paper, which simulated helium binding energy with high vacancy number (up to 20 vacancies) finding a strong interaction when $N_{He} < N_{vac}$. The original paper also shows good agreement with DFT results at low vacancy number. The value of ~6 eV for He in tungsten approaches He interstitial formation energy [65] with strong interaction between a single He and a void following a similar trend to He-cluster interaction with a He bubble as in [67] where a potential well equivalent to the formation energy of a He_4 cluster was seen for the cluster interacting with a He bubble. Voids would therefore act as a strong trapping site for He migrating in W, such as that migrating during the *in-situ* TEM irradiations and MD simulations.

The MD simulations in this study assumed that the voids would be formed by vacancy agglomeration during the initial W^{2+} beam exposure, and therefore very few monovacancies would be present in the inter-void spaces in the V structure. Effective He mobility in these 'damage-free' regions remains unaffected and is higher than that in the

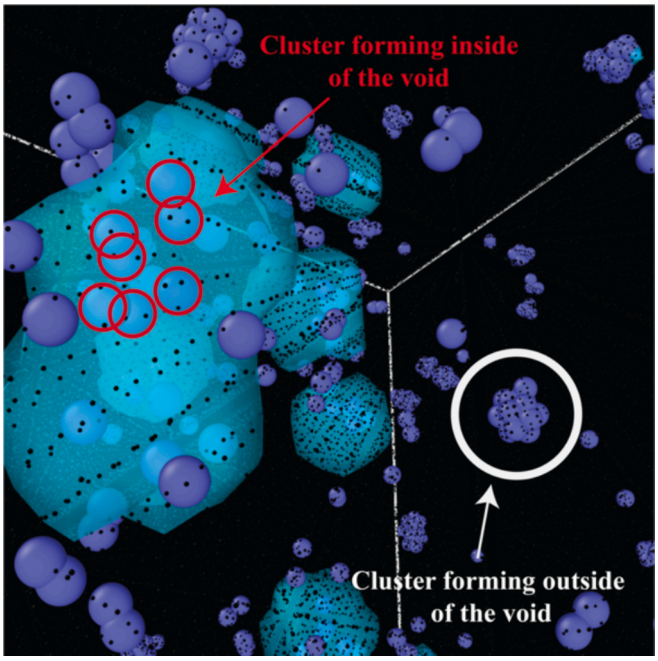

Fig. 8. Figure showing the clustering of helium both inside and outside of voids. The helium atoms are shown in purple, with the voids being shown in light blue. (For interpretation of the references to colour in this figure legend, the reader is referred to the web version of this article.)

porous cell. He migration to voids would therefore be easier, and He-He encounters for self-trapping would also not be inhibited. It should be noted that this latter effect is enhanced by the inherent high-flux nature of the simulations (~10^{26} m^{-2}). Attempts to compensate for this were made by enhancing the initial void density in the simulation (10^{25} m^{-3} simulated compared to ~10^{23} m^{-3} in experiment), thereby encouraging He-void interaction. The total cluster-to-void ratio at the end of the simulation was seen to be 20:1, demonstrating a clear preference for He-He cluster nucleation rather than voids being the nucleation sites. This suggested that despite the enhanced flux, there is therefore a strong possibility that self-affinity in reduced defect density areas was still causing cavity formation in the SQN irradiation. Overall, these simulations suggest that despite there being SIAs generated in the irradiations, the differences in the final cavity population could still be primarily attributed to the vacancy-helium interaction.

5. Conclusions

The interaction of large pre-existing cavities and smaller vacancy-type complexes with helium has been studied at 800 °C using *in-situ* TEM investigations under W^{2+}/He^{+} irradiation and supportive MD and MS simulations. W^{2+} irradiation to 0.256 dpa induces the formation of a cavity distribution in the W microstructure. The sequential (SQN) exposure to a He^{+} beam for an additional 0.095 dpa generated a lower number density distribution of cavities with a larger average diameter, as compared to concurrent (CON) irradiation. The large cavities in the SQN irradiation, formed during the initial W^{2+} irradiation, not only survive but also grow during the subsequent He^{+} irradiation, and those cavities become faceted at >0.063 dpa. In contrast, the simultaneous generation of vacancies and implanted He interstitials in the pristine W microstructure during a CON irradiation induced a fine distribution of small cavities after irradiation. Furthermore, MD simulations revealed the role of pre-existing cavities in attracting He atoms during cavity growth, further confirmed by the binding energies of ~6 eV obtained in MS simulations. Additional He-He clustering occurred in the vacancy-free inter-cavity space in the simulation structure. This implies that

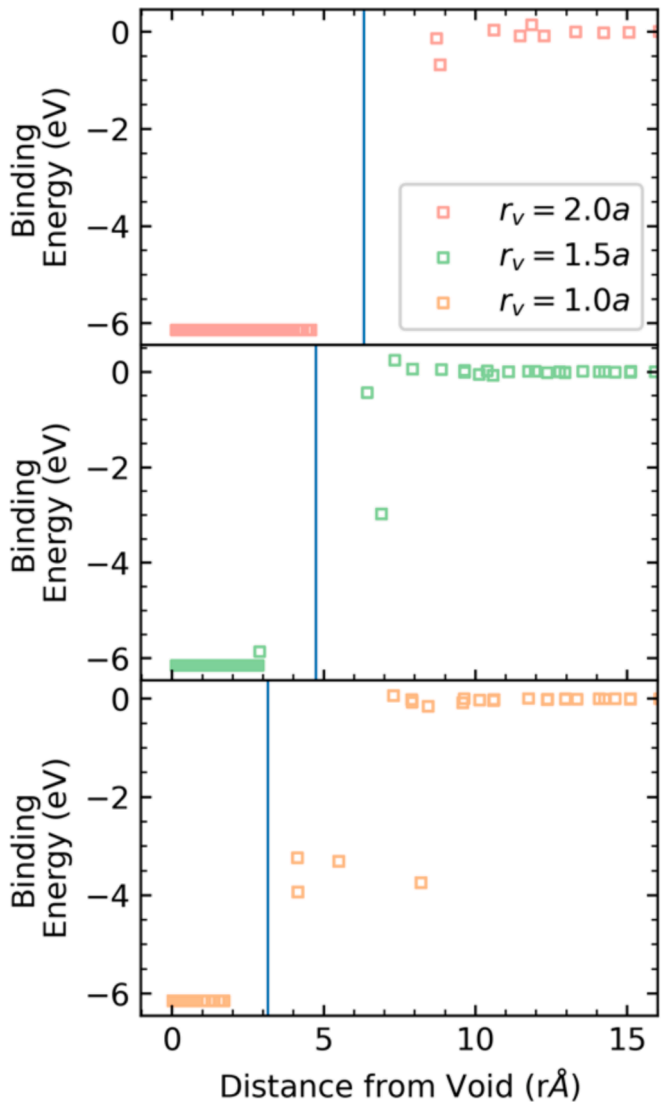

Fig. 9. Figure detailing the binding energy variation with distance from the void center. Lines in blue indicate the edge of the void, with all data points displayed on each graph. (For interpretation of the references to colour in this figure legend, the reader is referred to the web version of this article.)

the cavity binding energy for He is not sufficient to counteract He-He affinity and prevent self-trapping. In contrast, the presence of a fine distribution of porosity, simulant of the radiation-induced vacancy formation during W^{2+}+He^{+} CON irradiation, leads to a fine distribution of small cavities in the final structure due to a strong He-vac interaction and reduced He mobility. Consequently, the CON irradiation causes a higher density of cavities with a reduced average diameter.

CRediT authorship contribution statement

E. Yildirim: Writing – original draft, Methodology, Investigation, Formal analysis, Data curation, Conceptualization. **P.M. Mummery:** Writing – review & editing, Supervision, Resources, Funding acquisition. **G. Greaves:** Writing – review & editing, Resources, Investigation, Data curation. **C.P. Race:** Writing – review & editing, Methodology. **E. Jimenez-Melero:** Writing – review & editing, Supervision, Project administration, Funding acquisition.

Declaration of competing interest

The authors declare that they have no known competing financial interests or personal relationships that could have appeared to influence the work reported in this paper.

Data availability

I have attached a link in the supplementary materials file.

Acknowledgements

We wish to acknowledge the EPSRC support through grant number EP/L01663X/1, and the Henry Royce Institute through the Royce PhD Equipment Access Scheme for EY to access the Arc Melting facilities at Royce @Sheffield; EPSRC Grant Number EP/R00661X/1. CPR was supported by a University Research Fellowship of the Royal Society. Access to the MIAMI facility was provided through the UK national ion beam centre, EPSRC Grant Numbers EP/X015491/1 & EP/M028283/1.

Appendix A. Supplementary material

Supplementary data to this article can be found online at https://doi.org/10.1016/j.nme.2024.101672.

References

[1] R.A. Pitts et al., Physics basis for the first ITER tungsten divertor, in: Nuclear Materials and Energy, vol. 20, Elsevier Ltd, 2019, p. 100696, doi: 10.1016/j.nme.2019.100696.
[2] T. Hirai, et al., Use of tungsten material for the ITER divertor, Nucl. Mater. Energy 9 (2016) 616–622, https://doi.org/10.1016/j.nme.2016.07.003.
[3] M. Rieth, et al., Tungsten as a structural divertor material, in: 5th Forum on New Materials Part B, Trans Tech Publications Ltd, 2010, pp. 11–21, https://doi.org/10.4028/www.scientific.net/ast.73.11.
[4] Y. Ueda, et al., Research status and issues of tungsten plasma facing materials for ITER and beyond, Fus. Eng. Des. 89 (7–8) (2014) 901–906, https://doi.org/10.1016/j.fusengdes.2014.02.078.
[5] D. Terentyev, et al., Development of irradiation tolerant tungsten alloys for high temperature nuclear applications, Nucl. Fus. 62 (8) (2022) 086035, https://doi.org/10.1088/1741-4326/ac75fe.
[6] G. Federici, W. Biel, M.R. Gilbert, R. Kemp, N. Taylor, and R. Wenninger, European DEMO design strategy and consequences for materials Related content ITER conceptual design, 2017, doi: 10.1088/1741-4326/57/9/092002.
[7] D. Stork, et al., Materials R&D for a timely DEMO: Key findings and recommendations of the EU Roadmap Materials Assessment Group, Fus. Eng. Des. 89 (7–8) (2014) 1586–1594, https://doi.org/10.1016/j.fusengdes.2013.11.007.
[8] M.R. Gilbert, S.L. Dudarev, D. Nguyen-Manh, S. Zheng, L.W. Packer, J.-C. Sublet, Neutron-induced dpa, transmutations, gas production, and helium embrittlement of fusion materials, J. Nucl. Mater. 442 (1–3) (2013) S755–S760, https://doi.org/10.1016/j.jnucmat.2013.03.085.
[9] J. Varje, et al., Effect of plasma response on the fast ion losses due to ELM control coils in ITER, Nucl. Fus. 56 (4) (2016) 046014, https://doi.org/10.1088/0029-5515/56/4/046014.
[10] V. Kotov, A. Litnovsky, A.S. Kukushkin, D. Reiter, A. Kirschner, Numerical modelling of steady-state fluxes at the ITER first wall, J. Nucl. Mater. 390–391 (2009) 528–531, https://doi.org/10.1016/j.jnucmat.2009.01.301.
[11] H. Ullmaier, The influence of helium on the bulk properties of fusion reactor structural materials, Nucl. Fus. 1039 (24) (1984).
[12] F. Hofmann, M. Short, C. Dennett, Transient grating spectroscopy: sn ultrarapid, nondestructive materials evaluation technique, MRS Bull. 44 (5) (2019), https://doi.org/10.1557/mrs.2019.104.
[13] T. Miyazawa, et al., Effects of helium on mechanical properties of tungsten for fusion applications, Nucl. Mater. Energy 15 (2018) 154–157, https://doi.org/10.1016/j.nme.2018.04.003.
[14] A. Hasegawa, et al., Helium effects on tensile properties of powder metallurgical-processed tungsten for fusion reactor applications, Nucl. Mater. Energy 29 (2021), https://doi.org/10.1016/j.nme.2021.101076.
[15] M.S. Abd, E. Keriem, D.P. Van Der Werf, F. Pleiter, Helium-vacancy interaction in tungsten, 1993.
[16] K.O.E. Henriksson, K. Nordlund, J. Keinonen, Molecular dynamics simulations of helium cluster formation in tungsten, Nucl. Instrum. Methods Phys. Res. B 244 (2) (2006) 377–391, https://doi.org/10.1016/j.nimb.2005.10.020.
[17] K.O.E. Henriksson, K. Nordlund, A. Krasheninnikov, J. Keinonen, Difference in formation of hydrogen and helium clusters in tungsten, Appl. Phys. Lett. 87 (16) (2005) 1–3, https://doi.org/10.1063/1.2103390.
[18] D. Jeannotte, J.M. Galligan, Energy of motion of vacancies in tungsten, 1967.

[19] M.W. Thompson, The damage and recovery of neutron irradiated tungsten, Philos. Mag. 5 (51) (1960) 278–296, https://doi.org/10.1080/14786436008235842.
[20] M.J. Lloyd, et al., Decoration of voids with rhenium and osmium transmutation products in neutron irradiated single crystal tungsten, Scr. Mater. 173 (2019) 96–100, https://doi.org/10.1016/j.scriptamat.2019.07.036.
[21] X. Hu, Recent progress in experimental investigation of neutron irradiation response of tungsten, J. Nucl. Mater. 568 (2022).
[22] O. El-Atwani, et al., Loop and void damage during heavy ion irradiation on nanocrystalline and coarse grained tungsten: Microstructure, effect of dpa rate, temperature, and grain size, Acta Mater. 149 (2018) 206–219, https://doi.org/10.1016/j.actamat.2018.02.035.
[23] W. Jiang, et al., Dose rate effects on damage accumulation and void growth in self-ion irradiated tungsten, J. Nucl. Mater. 550 (2021), https://doi.org/10.1016/j.jnucmat.2021.152905.
[24] A. Hasegawa, M. Fukuda, K. Yabuuchi, S. Nogami, Neutron irradiation effects on the microstructural development of tungsten and tungsten alloys, J. Nucl. Mater. 471 (2016) 175–183, https://doi.org/10.1016/j.jnucmat.2015.10.047.
[25] M. Fukuda, K. Yabuuchi, S. Nogami, A. Hasegawa, T. Tanaka, Microstructural development of tungsten and tungsten-rhenium alloys due to neutron irradiation in HFIR, J. Nucl. Mater. 455 (1–3) (2014) 460–463, https://doi.org/10.1016/j.jnucmat.2014.08.002.
[26] M. Fukuda, et al., Neutron energy spectrum influence on irradiation hardening and microstructural development of tungsten, J. Nucl. Mater. 479 (2016) 249–254, https://doi.org/10.1016/j.jnucmat.2016.06.051.
[27] J.C. He, A. Hasegawa, K. Abe, Effects of transmutation elements on the defect structure development of W irradiated by protons and neutrons, J. Nucl. Mater. 377 (2) (2008) 348–351, https://doi.org/10.1016/j.jnucmat.2008.03.014.
[28] M.J. Lloyd, et al., Interaction of transmutation products with precipitates, dislocations and grain boundaries in neutron irradiated W, Materialia (Oxf) 22 (2022) 101370, https://doi.org/10.1016/j.mtla.2022.101370.
[29] G.S. Was, Challenges to the use of ion irradiation for emulating reactor irradiation, J. Mater. Res. 30 (9) (2015), https://doi.org/10.1557/jmr.2015.73.
[30] G. Greaves, A.H. Mir, R.W. Harrison, M.A. Tunes, S.E. Donnelly, J.A. Hinks, New Microscope and Ion Accelerators for Materials Investigations (MIAMI-2) system at the University of Huddersfield, Nucl. Instrum. Methods Phys. Res. A 931 (2019) 37–43, https://doi.org/10.1016/j.nima.2019.03.074.
[31] J.A. Hinks, Transmission electron microscopy with in situ ion irradiation, J. Mater. Res. 30 (9) (2015) 1214–1221, https://doi.org/10.1557/jmr.2014.384.
[32] S. Ishino, In-situ observation of radiation damage using a combined facility of electron microscope and heavy-ion accelerator(s): history and future prospectives, Mater. Trans. 55 (3) (2014) 396–402, https://doi.org/10.2320/matertrans.MD201304.
[33] M. Li, M.A. Kirk, P.M. Baldo, D. Xu, B.D. Wirth, Study of defect evolution by TEM with in situ ion irradiation and coordinated modeling, Philos. Mag. 92 (16) (2012) 2048–2078, https://doi.org/10.1080/14786435.2012.662601.
[34] H. Iwakiri, K. Yasunaga, K. Morishita, N. Yoshida, Microstructure evolution in tungsten during low-energy helium ion irradiation, J. Nucl. Mater. 283–287 (2000) 1134–1138, https://doi.org/10.1016/S0022-3115(00)00289-0.
[35] R.W. Harrison, G. Greaves, J.A. Hinks, S.E. Donnelly, A study of the effect of helium concentration and displacement damage on the microstructure of helium ion irradiated tungsten, J. Nucl. Mater. 495 (2017) 492–503, https://doi.org/10.1016/j.jnucmat.2017.08.033.
[36] Y. Li, et al., In-situ TEM investigation of 30 keV he+ irradiated tungsten: effects of temperature, fluence, and sample thickness on dislocation loop evolution, Acta Mater. 206 (2021) 116618, https://doi.org/10.1016/j.actamat.2020.116618.
[37] R.W. Harrison, H. Amari, G. Greaves, J.A. Hinks, S.E. Donnelly, Effect of He-appm/DPA ratio on the damage microstructure of tungsten, MRS Advances 1 (42) (2016) 2893–2899, https://doi.org/10.1557/adv.2016.385.
[38] S. Hasanzadeh, et al., Three-dimensional scanning transmission electron microscopy of dislocation loops in tungsten, Micron 113 (2018) 24–33, https://doi.org/10.1016/j.micron.2018.05.010.
[39] I. Ipatova, G. Greaves, S. Pacheco-Gutiérrez, S.C. Middleburgh, M.J.D. Rushton, E. Jimenez-Melero, In-situ TEM investigation of nano-scale helium bubble evolution in tantalum-doped tungsten at 800°C, J. Nucl. Mater. 550 (2021), https://doi.org/10.1016/j.jnucmat.2021.152910.
[40] O. El-Atwani, et al., In-situ TEM observation of the response of ultrafine- and nanocrystalline-grained tungsten to extreme irradiation environments, Sci. Rep. 4 (1) (2014) 4716, https://doi.org/10.1038/srep04716.
[41] O. El-Atwani, et al., Temperature threshold for preferential bubble formation on grain boundaries in tungsten under in-situ helium irradiation, Scr. Mater. 180 (2020) 6–10, https://doi.org/10.1016/j.scriptamat.2020.01.013.
[42] O. El-Atwani, W.S. Cunningham, J.R. Trelewicz, M. Li, B.D. Wirth, S.A. Maloy, Revealing the synergistic effects of sequential and simultaneous dual beam irradiations in tungsten via in-situ TEM, J. Nucl. Mater. 538 (2020), https://doi.org/10.1016/j.jnucmat.2020.152150.
[43] J.F. Ziegler, M.D. Ziegler, J.P. Biersack, SRIM – the stopping and range of ions in matter (2010), Nucl. Instrum. Methods Phys. Res. B 268 (11–12) (2010) 1818–1823, https://doi.org/10.1016/j.nimb.2010.02.091.
[44] J.F. Ziegler, Stopping of energetic light ions in elemental matter, J. Appl. Phys. 85 (3) (1999) 1249–1272, https://doi.org/10.1063/1.369844.
[45] R.E. Stoller, M.B. Toloczko, G.S. Was, A.G. Certain, S. Dwaraknath, F.A. Garner, On the use of SRIM for computing radiation damage exposure, Nucl. Instrum. Methods Phys. Res. B 310 (2013) 75–80, https://doi.org/10.1016/j.nimb.2013.05.008.
[46] ASTM E521-96, Standard practice for neutron radiation damage simulation by charged-particle irradiation, 2009.
[47] D.B. Williams, C.B. Carter, Transmission Electron Microscopy: Diffraction, Imaging and Spectroscopy, second edition, Springer, 2016.
[48] M.L. Jenkins, M.A. Kirk, Characterization of Radiation Damage by Transmission Electron Microscopy, first edition, Institute of Physics Publishing, Bristol, 2001.
[49] J. Schindelin, et al., Fiji: an open-source platform for biological-image analysis, Nat. Methods 9 (7) (2012) 676–682, https://doi.org/10.1038/nmeth.2019.
[50] S. Plimpton, Fast parallel algorithms for short-range molecular dynamics, J. Comput. Phys. 117 (1) (1995) 1–19, https://doi.org/10.1006/jcph.1995.1039.
[51] A.P. Thompson, et al., LAMMPS - a flexible simulation tool for particle-based materials modeling at the atomic, meso, and continuum scales, Comput. Phys. Commun. 271 (2022), https://doi.org/10.1016/j.cpc.2021.108171.
[52] D.R. Mason, D. Nguyen-Manh, C.S. Becquart, An empirical potential for simulating vacancy clusters in tungsten, J. Phys. Condensed Matter 29 (50) (2017), https://doi.org/10.1088/1361-648X/aa9776.
[53] N. Juslin, B.D. Wirth, Interatomic potentials for simulation of He bubble formation in W, J. Nucl. Mater. 432 (1–3) (2013) 61–66, https://doi.org/10.1016/j.jnucmat.2012.07.023.
[54] K. Morishita, R. Sugano, B.D. Wirth, T. Diaz de la Rubia, Thermal stability of helium-vacancy clusters in iron, Nucl. Instrum. Methods Phys. Res. Sect. B: Beam Interact. Mater. Atoms (2003) 76–81, https://doi.org/10.1016/S0168-583X(02)01832-3.
[55] F. Sefta, N. Juslin, B.D. Wirth, Helium bubble bursting in tungsten, J. Appl. Phys. 114 (24) (2013) 243518, https://doi.org/10.1063/1.4860315.
[56] K.D. Hammond, S. Blondel, L. Hu, D. Maroudas, B.D. Wirth, Large-scale atomistic simulations of low-energy helium implantation into tungsten single crystals, Acta Mater. 144 (2018) 561–578, https://doi.org/10.1016/j.actamat.2017.09.061.
[57] D. Perez, L. Sandoval, S. Blondel, B.D. Wirth, B.P. Uberuaga, A.F. Voter, The mobility of small vacancy/helium complexes in tungsten and its impact on retention in fusion-relevant conditions, Sci. Rep. 7 (1) (2017), https://doi.org/10.1038/s41598-017-02428-2.
[58] F. Ferroni, X. Yi, K. Arakawa, S.P. Fitzgerald, P.D. Edmondson, S.G. Roberts, High temperature annealing of ion irradiated tungsten, Acta Mater. 90 (2015) 380–393, https://doi.org/10.1016/j.actamat.2015.01.067.
[59] X.C. Li, Y.N. Liu, Y. Yu, G.N. Luo, X. Shu, G.H. Lu, Helium defects interactions and mechanism of helium bubble growth in tungsten: a molecular dynamics simulation, J. Nucl. Mater. 451 (1–3) (2014) 356–360, https://doi.org/10.1016/j.jnucmat.2014.04.022.
[60] Z.-Z. Li, et al., Investigating the formation mechanism of void lattice in tungsten under neutron irradiation: from collision cascades to ordered nanovoids, Acta Mater. 219 (2021) 117239, https://doi.org/10.1016/j.actamat.2021.117239.
[61] R.W. Harrison, N. Peng, R.P. Webb, J.A. Hinks, S.E. Donnelly, Characterisation of helium ion irradiated bulk tungsten: a comparison with the in-situ TEM technique, Fus. Eng. Des. 138 (2019) 210–216, https://doi.org/10.1016/j.fusengdes.2018.11.024.
[62] Z. Yang, S. Blondel, K.D. Hammond, B.D. Wirth, Kinetic Monte Carlo simulations of helium cluster nucleation in tungsten with preexisting vacancies, Fus. Sci. Technol. 71 (1) (2017) 60–74, https://doi.org/10.13182/FST16-111.
[63] C.S. Becquart, C. Domain, An object Kinetic Monte Carlo Simulation of the dynamics of helium and point defects in tungsten, J. Nucl. Mater. 385 (2) (2009) 223–227, https://doi.org/10.1016/j.jnucmat.2008.11.027.
[64] C.S. Becquart, C. Domain, Ab initio calculations about intrinsic point defects and He in W, Nucl. Instrum. Methods Phys. Res. B 255 (1) (2007) 23–26, https://doi.org/10.1016/j.nimb.2006.11.006. SPEC. ISS.
[65] S.C. Lee, J.H. Choi, J.G. Lee, Energetics of He and H atoms with vacancies in tungsten: first-principles approach, J. Nucl. Mater. 383 (3) (2009) 244–246, https://doi.org/10.1016/j.jnucmat.2008.09.017.
[66] P.E. Lhuillier, et al., Helium retention and early stages of helium-vacancy complexes formation in low energy helium-implanted tungsten, J. Nucl. Mater. 433 (1–3) (2013) 305–313, https://doi.org/10.1016/j.jnucmat.2012.09.001.
[67] A. Weerasinghe, L. Hu, K.D. Hammond, B.D. Wirth, D. Maroudas, Non-dilute helium-related defect interactions in the near-surface region of plasma-exposed tungsten, J. Appl. Phys. 128 (16) (2020), https://doi.org/10.1063/5.0023356.